Available online at www.sciencedirect.com
ScienceDirect
Trans. Nonferrous Met. Soc. China 32(2022) 3259−3275

Transactions of
Nonferrous Metals
Society of China
www.tnmsc.cn

Hot workability and dynamic recrystallization mechanisms of pure nickel N6

Zhi JIA[1,2], Bao-lin WEI[1], Xuan SUN[1], Jin-jin JI[3], Yan-jiang WANG[1], Li-dan YU[1]

1. School of Materials Science and Engineering, Lanzhou University of Technology, Lanzhou 730050, China;
2. State Key Laboratory of Advanced Processing and Recycling of Nonferrous Metals,
Lanzhou University of Technology, Lanzhou 730050, China;
3. School of Materials Engineering, Lanzhou Institute of Technology, Lanzhou 730050, China

Received 18 June 2021; accepted 9 December 2021

Abstract: The hot workability and dynamic recrystallization (DRX) mechanisms of pure nickel N6 were systematically investigated using hot compression tests. Based on hot compression data, the constitutive equation of N6 was developed and its reliability was verified. Its hot processing map was constructed, and combined with microstructural observations, a semi-quantitative response relationship between hot deformation parameters and microstructure was established. The DRX process of N6 is a thermally activated process and particularly sensitive to the strain rate. The optimal hot processing parameters for N6 were determined to be 950−1050 °C and 0.1−1 s^{-1}. Furthermore, it was proven that the dominant nucleation mechanism is discontinuous DRX characterized by grain boundary bulging and twins assisting nucleation, while the continuous DRX characterized by subgrains combined with rotation is an inactive nucleation mechanism.

Key words: pure nickel N6; microstructure evolution; hot workability; processing map; dynamic recrystallization

1 Introduction

N6 is widely used in the alkali industry due to its incomparably superior corrosion resistance to high temperature and high concentrations of caustic alkali. Its large thick-walled pipes are mostly used in evaporators, heaters, lye storage tanks, pipelines, pumps, and valves in the alkali industry [1−3]. However, current research focuses on nickel-based alloys. The mechanical properties of N6 are lower than those of other nickel-based alloys, which limits its application in practical engineering [4,5]. Therefore, the lack of systematic and in-depth research on N6 leads to unclear mechanisms of microstructure transformation of its tubes, which seriously restricts the performance improvement of relevant equipment and the demand for high-quality pure nickel tubes and bars. The hot forming process is an optimal method to manufacture N6 tubes or tube components. Similar to many nickel-based superalloys, the thermal deformation of N6 is characterized by complex dynamic recrystallization (DRX) structural evolution, which is sensitive to the deformation temperature, strain rate, and strain [6−10]. Therefore, reasonable process parameters are necessary to achieve high-quality manufacturing of N6 pipes or pipe components.

The constitutive model and processing map based on the dynamic material model (DMM) are key components in understanding the thermal deformation behavior of the material [11−15]. In recent years, many scholars have used the classic Arrhenius hyperbolic sine formula and processing maps to predict the high temperature deformation behavior of various nickel-based alloys, such as GH4169 alloy [11], 80A alloy [12], GH4698 alloy [13], GH696 alloy [14], and Inconel 625 [15].

Corresponding author: Zhi JIA, Tel: +86-18293167033, E-mail: jiazhi@lut.edu.cn
DOI: 10.1016/S1003-6326(22)66018-7

DRX is the main softening mechanism of nickel-based alloys with lower stacking fault energy (SFE). In previous studies, the conventional discontinuous dynamic recrystallization (DDRX) characterized the local bulge of grain boundaries as the main nucleation mechanism in nickel-based alloys [16−19]. In addition, twins can also promote the nucleation of the nickel-based alloys by accelerating the protrusion of the original grain boundary and the subsequent separation of the protrusion from other grain boundaries [20,21]. On the other hand, the continuous dynamic recrystallization (CDRX), characterized by the progressive rotation of subgrains, has also been shown in other nickel-based superalloys over the past few years. Although CDRX is considered to occur easily in high SFE metal materials [17,22−26], there is no consensus on the favorable deformation conditions of CDRX in nickel-based superalloys. Therefore, an in-depth understanding of the hot forming behavior and DRX mechanism in the N6 hot deformation process is urgently needed.

In this study, the hot deformation behavior and DRX mechanism of N6 alloys were studied through a series of isothermal compression experiments. Based on a constitutive model and hot processing map, the hot deformation behavior of N6 was studied. The focus was on the DRX mechanism in hot deformation of N6, and the typical micro-structures involved in different DRX mechanisms were discussed in depth.

2 Experimental

The nominal chemical compositions (wt.%) of N6 are 0.047C−0.05Mn−0.018Si−0.064Cu−0.3Co−0.046Al−0.11Fe−0.018Ti−0.045S and balanced Ni. The specimens of d8 mm × 12 mm were taken from a hot rolled billet. Figure 1(a) shows the typical metallographic microstructure of N6, which consists of nearly equiaxed, static recrystallization (SRX) grains (yellow) and a multitude of annealing twins (Fig. 1(b)). The hot deformation tests were performed on a Gleeble−3500 thermal simulator, which were carried out over a temperature range of 900−1200 °C (in increments of 100 °C) and strain rates of 0.01−10 s^{-1} with a true strain of 0.7. The hot compression process scheme is shown in Fig. 1(c).

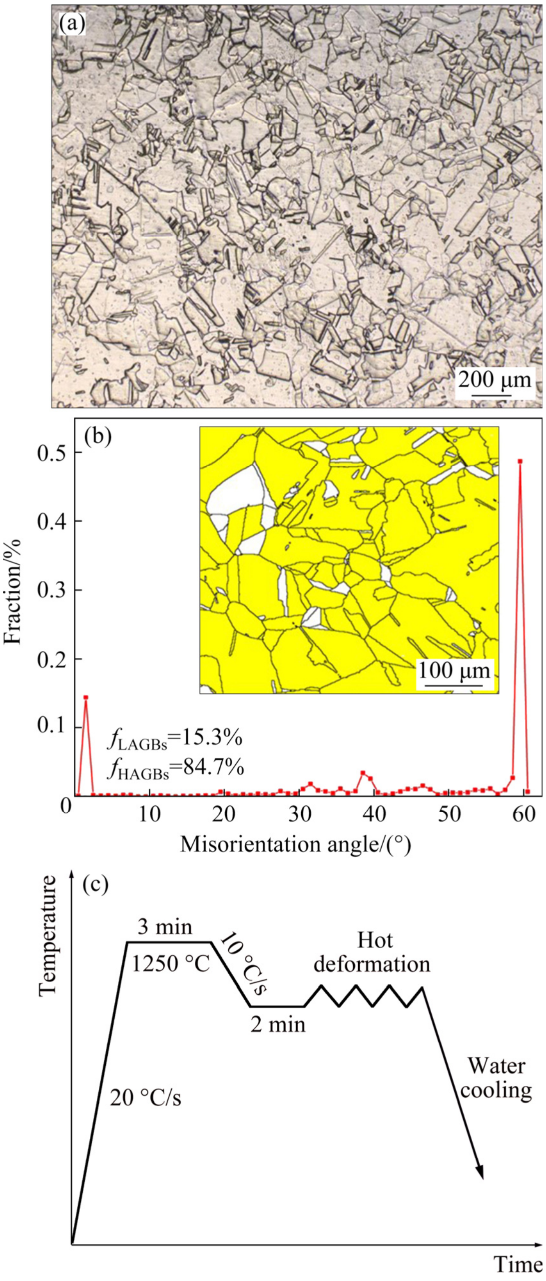

Fig. 1 Metallographic microstructure of N6 (a), micro-structure of N6 characterized by EBSD (b) and hot compression process scheme (c)

After hot compression, the specimens were cut along the compression axis with the EDM wire cutting equipment for microstructural analysis. The observation location was in the central region of the section mentioned above. The metallographic specimens were ground using various grits of sandpaper ($400^{\#}$ to $3000^{\#}$). Afterwards, the specimens were polished using a 0.5 μm diamond solution and etched in a solution of 3 mL HNO_3 + 5 mL $C_2H_4O_2$ for 30 s, and then observed using an LSM 800 optical light microscope. For electron backscatter diffraction (EBSD) analysis, samples were electropolished in a solution of 90mL C_2H_5OH + 10 mL $HClO_4$ at −20 °C and a voltage of 50 V. The EBSD measurements and analyses were completed using the HKL system mounted in an FEI NovaNano SEM 430. The sample microstructure was characterized on the compression direction−transverse direction (CD−TD) cross section. The microstructure of the sample at 900 °C and 1 s^{-1} was observed by TEM (JEM−2100) with a working voltage of 200 kV. The TEM sample was first sliced to a thickness of about 50 μm by sandpaper and then punched into 3 mm diameter discs. This was followed by double-jet electrolytic polishing at 0 °C using an electrolyte consisting of 90 mL C_2H_5OH and 10 mL $HClO_4$.

3 Results

3.1 Hot deformation behavior

Figure 2 shows the true stress−true strain curves of the N6 after hot compression test. It can be seen that, at strain rate ≤1 s^{-1}, the stress level increases rapidly to a peak value with increasing strain, then decreases, and finally reaches steady state. This trend corresponds to three distinct stages: work hardening, softening process, and stability [6,15,27]. In the initial stage of deformation, work hardening plays a primary role, which causes dislocations to increase and rapidly accumulate, leading to a rapid increase in flow stress. DRX occurs when the dislocations accumulate to a value [28]. The action of DRX gradually reduces the flow stress. Under the combined action of work intensification and DRX, the flow stress reaches a stable state. The rheological curve of N6 shows obvious DRX characteristics.

At a high strain rate (10 s^{-1}), the flow stress shows a tendency to increase firstly and then decrease, and it is difficult to reach a steady-state rheological state. This may be due to the short deformation time of high strain rate (10 s^{-1}), the instantaneous change of stress and strain, and the generation of deformation heat, but the deformation heat does not have enough time to conduct outwards, resulting in a significant temperature increase in some areas. This phenomenon is called

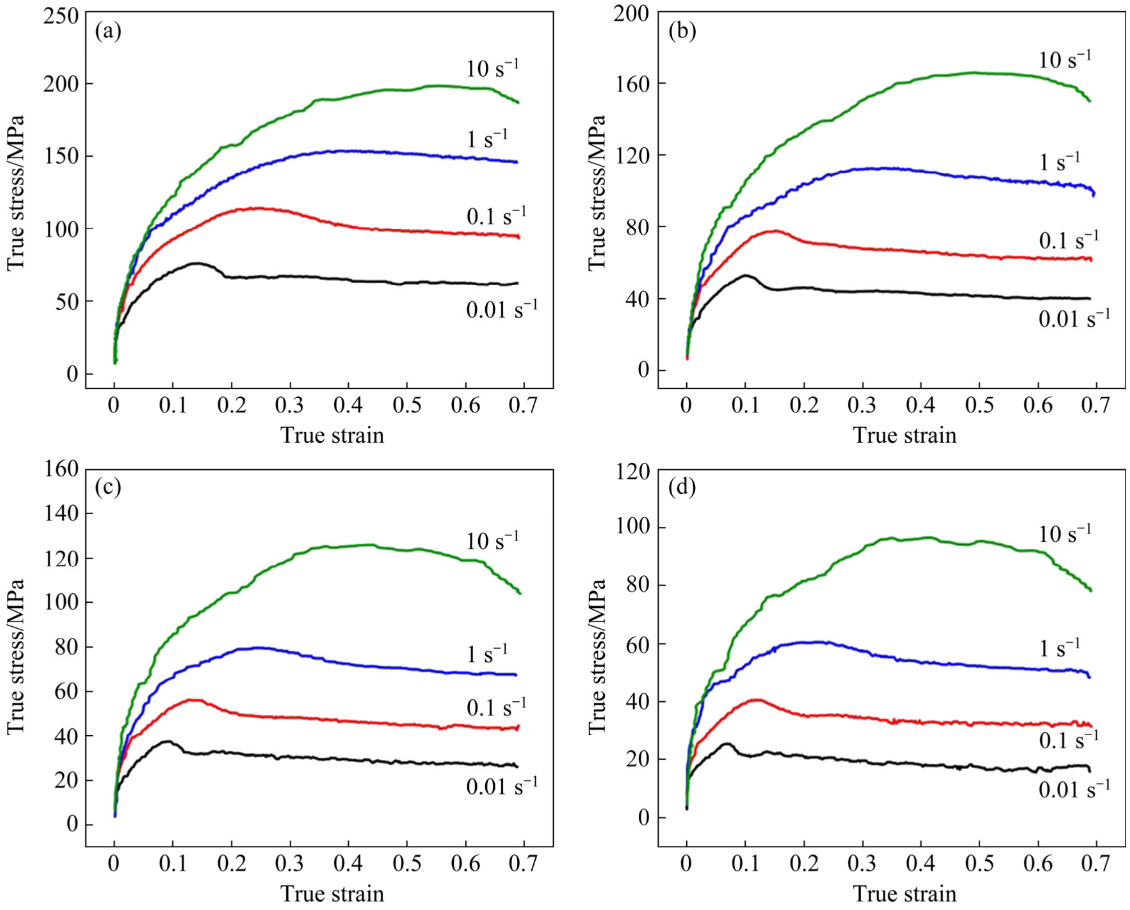

Fig. 2 True stress−true strain curves of N6: (a) 900 °C; (b) 1000 °C; (c) 1100 °C; (d) 1200 °C

the adiabatic temperature rise (ATR) effect [29]. The heat of deformation can be estimated using the following formula:

$$\Delta T=\frac{\eta_1\int\sigma \mathrm{d}\varepsilon}{\rho c_p} \tag{1}$$

where ΔT is the adiabatic temperature rise, $\int\sigma\mathrm{d}\varepsilon$ is the work of plastic deformation, ρ is the density of the material, c_p is the specific heat capacity of the material, and η_1 is the adiabatic factor, which is generally equal to 0.9. The adiabatic temperature rise as a function of strain at different temperatures and a strain rate of 10 s^{-1} is shown in Fig. 3(a).

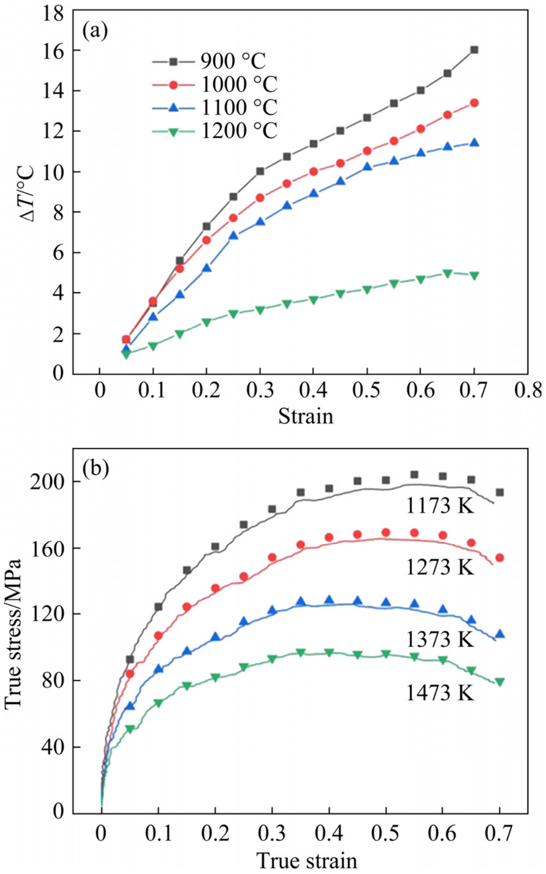

Fig. 3 Adiabatic temperature rise at different temperatures and strain rate of 10 s^{-1} (a), and adiabatic temperature rise corrected stress curves (b)

The ATR phenomenon leads to changes in the measured flow stress, which should be corrected for temperature rise [30]. The influence of temperature rise on stress is expressed by Eq. (2):

$$\Delta\sigma=\frac{Q\left(\frac{1}{T}-\frac{1}{T+\Delta T}\right)}{Rn\alpha} \tag{2}$$

where $\Delta\sigma$ is the stress difference caused by adiabatic temperature rise, MPa; Q is the activation energy of hot deformation, kJ/mol; R is the molar gas constant with a value of 8.314 J/(mol·K); T is the deformation temperature, K; n is the stress index; α is the parameter used to describe the rheological properties of the material when it is deformed at high temperature.

According to Eq. (2), the corresponding stress value at the actual temperature can be obtained, as shown in Fig. 3(b). To reduce the number of calculations, only the experimental points whose true strain value is an integer multiple of 0.05 are used to correct the stress and temperature rise.

Using metals as an example, the Johnson–Cook (JC) model has become a widely used phenomeno-logical model to describe a material's stress–strain response with both strain rate and temperature effects [31]. The JC model describes how the material is softened with respect to temperature but does not directly indicate how the temperature increases. This results in a relatively implicit relationship between strain rate and the thermal softening effect [32]. Although efforts have been made to solve the thermal softening effect in a more explicit way using the JC model, the results of the research are inconsistent. Many authors relate the adiabatic rise in temperature with a low fraction of twinning at high strain rate compression [33,34]. Other authors mentioned that there is a strong positive correlation between the ATR value and the strain rate, but there is a strong negative correlation between the ATR value and the deformation temperature [35]. Based on the experimental foundation and experience of the predecessors, this research has carried out corresponding calculations and corrections on the influence of the adiabatic temperature rise effect.

3.2 Constitutive modeling of hot deformation

The constitutive equation expresses the relationship between flow stress, deformation temperature, and strain rate under hot working conditions, which is the dynamic response to the material deformation process [31]. This study uses the Arrhenius hyperbolic sine function model to describe the general form of the function. These equations are shown as follows [29]:

$$\dot{\varepsilon}=A_1\sigma^{n_1}\exp[-Q/(RT)],\ \text{for } \alpha\sigma<0.8 \tag{3}$$

$$\dot{\varepsilon}=A_2\exp(\beta\sigma)\cdot\exp[-Q/(RT)],\ \text{for } \alpha\sigma>1.2 \tag{4}$$

$$\dot{\varepsilon}=A[\sinh(\alpha\sigma)]^{n}\exp[-Q/(RT)],\ \text{for all } \alpha\sigma \tag{5}$$

where $\dot{\varepsilon}$ is the strain, s^{-1}; A is the structure factor, s^{-1}; α is the stress level parameter, MPa^{-1}; σ is the stress, MPa; A_1, A_2, n_1 and β are all constants after conversion, and $\alpha=\beta/n_1$.

Using peak stress σ_p as the input data, the unknown constant parameter in the equation is obtained by the linear regression method. By taking the natural logarithms for both sides of Eqs. (3)−(5), the following equations are obtained:

$$n_1=\left[\frac{\partial \ln \dot{\varepsilon}}{\partial \ln \sigma_p}\right]_{T=\text{constant}} \tag{6}$$

$$\beta=\left[\frac{\partial \ln \dot{\varepsilon}}{\partial \sigma_p}\right]_{T=\text{constant}} \tag{7}$$

$$n=\left[\frac{\partial \ln \dot{\varepsilon}}{\partial \ln[\sinh(\alpha\sigma)]}\right]_{T=\text{constant}} \tag{8}$$

Figure 4 shows the peak stress of N6 at different temperatures and strain rates during high-temperature compression. As seen from the above formulae, the values of n_1 and β can be obtained through the relationship between $\ln\sigma-\ln\dot{\varepsilon}$ and $\sigma-\ln\dot{\varepsilon}$. Linear regression analysis is performed on Eqs. (6) and (7) according to the peak stress measured by the hot compression experiment, and the linear relationships of $\ln\sigma-\ln\dot{\varepsilon}$ and $\sigma-\ln\dot{\varepsilon}$ are fitted, respectively, as shown in Figs. 5(a) and (b). The values of n_1 and β are equal to the reciprocal of the mean of each slope in the graphs. Therefore, n_1=6.07632 and β=0.07414 MPa^{-1}. Based on $\alpha=\beta/n_1$, α=0.0122 MPa^{-1} can be obtained, the value of n can be determined from the relationship of $\ln[\sinh(\alpha\sigma)]-\ln\dot{\varepsilon}$ (Fig. 5(c)), and the average value of n is equal to the reciprocal of the mean of each

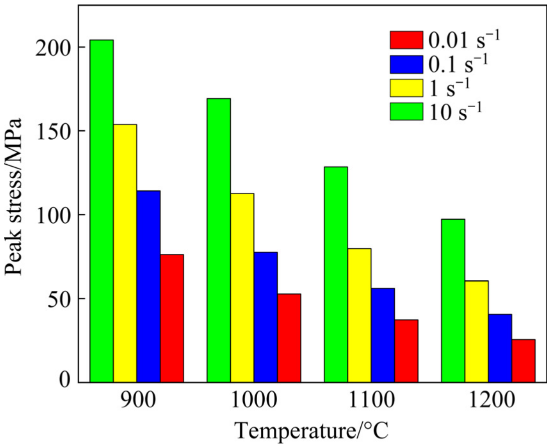

Fig. 4 Peak stress during hot compression of N6

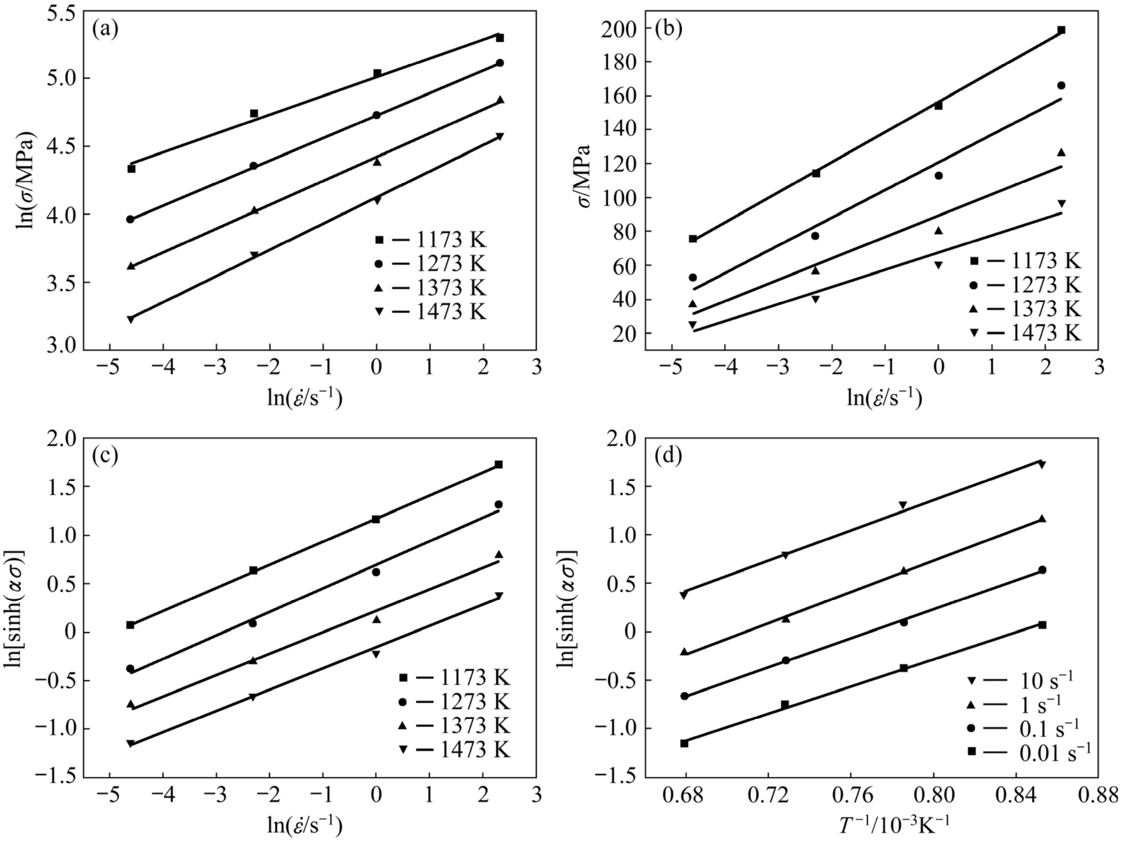

Fig. 5 Linear fitting relationships of $\ln\sigma-\ln\dot{\varepsilon}$ (a), $\sigma-\ln\dot{\varepsilon}$ (b), $\ln[\sinh(\alpha\sigma)]-\ln\dot{\varepsilon}$ (c), $\ln[\sinh(\alpha\sigma)-T^{-1}$ (d)

slope in the graph. Therefore, n=4.355 is obtained.

Taking the natural logarithm of both sides of Eq. (5), the following equation can be obtained:

$$\ln\dot{\varepsilon}=\ln A+n\ln[\sinh(\alpha\sigma)]-Q/(RT) \tag{9}$$

According to Eq. (9), it can be found that the intercept of the fitted straight line $\ln[\sinh(\alpha\sigma)]-\ln\dot{\varepsilon}$ is $\ln A$, so the value of structure factor A can be obtained. From Fig. 5(c), the average intercept of the four fitted straight lines can be calculated to be 22.907, that is, $\ln A$=22.907, and then A= $8.879\times10^{9}\ \mathrm{s}^{-1}$.

Taking the partial differential equation of both sides of Eq. (9), the activation energy of hot deformation can be obtained from the following equation:

$$Q=R\left[\frac{\partial\ln\dot{\varepsilon}}{\partial\ln[\sinh(\alpha\sigma)]}\bigg|_{T=\text{constant}}\right]\cdot\left[\frac{\partial\ln[\sinh(\alpha\sigma)]}{\partial T^{-1}}\bigg|_{\dot{\varepsilon}=\text{constant}}\right] \tag{10}$$

where $\left[\frac{\partial\ln\dot{\varepsilon}}{\partial\ln[\sinh(\alpha\sigma)]}\bigg|_{T=\text{constant}}\right]$=$n$=4.355. In the same way, the value of Q can be determined from the relationship of $\ln[\sinh(\alpha\sigma)]-T^{-1}$ (Fig. 5(d)). According to Eq. (10), the activation energy of hot deformation Q=272.988 kJ/mol.

Compared with other nickel-based superalloys, pure nickel N6 has a lower hot deformation activation energy. For example, the hot deformation activation energy of Ni80A alloy is 405.57 kJ/mol [36]. When the strain is 0.20−0.60, the apparent activation energy of hot deformation of GH696 superalloy is in the range of 389.524−410.236 kJ/mol [14]. The average activation energy for the hot deformation of Inconel 740 alloy at 1000−1200 °C is 373.86 kJ/mol [37]. This is mainly because the addition of other elements in the alloy results in a dislocation movement and thermodynamic mechanism different from that of N6. When the elements of the alloy are determined, the hot deformation activation energy is mainly related to the deformation temperature and strain rate, so the calculated Q value above is the average value of N6 in the range of 900−1200 °C.

According to the above derivation, the constitutive equation in the hot deformation process of N6 can be obtained as follows:

$$\dot{\varepsilon}=8.879\times10^{9}[\sinh(0.0122\sigma)]^{4.355}\cdot\exp[-272.988/(RT)] \tag{11}$$

3.3 Hot processing map

To assess the hot workability of the tested N6, a hot deformation processing map was considered based on the DMM [38,39]. Under the conditions of constant temperature and strain rate, the constitutive relationship of the material in the hot deformation process can be expressed as

$$\sigma=K\dot{\varepsilon}^{m} \tag{12}$$

where K is a constant and m is the strain rate sensitive factor, which can expressed as the distribution coefficient between the energy consumed by plastic deformation (J) and the energy consumed by tissue changes (G). m can be expressed as the following relationship [40]:

$$m=\left(\frac{\partial J}{\partial G}\right)_{\varepsilon,T}=\left[\frac{\partial(\ln\sigma)}{\partial(\ln\dot{\varepsilon})}\right]_{\varepsilon,T}=\left(\frac{\dot{\varepsilon}\,\partial\sigma}{\sigma\,\partial\dot{\varepsilon}}\right)_{\varepsilon,T} \tag{13}$$

The power dissipated for microstructure evolution is reflected by power dissipation efficiency η, which is a function of strain rate sensitivity [40]:

$$\eta=\frac{2m}{m+1} \tag{14}$$

The stress value at a true strain of 0.5 is extracted from the hot compression data to a series of derivation calculations, where the power dissipation map can be drawn on the plane formed by the deformation temperature T and the strain rate $\dot{\varepsilon}$ (Fig. 6(a)).

Only relying on the power dissipation map is not enough to accurately and effectively judge the processing performance of the corresponding parameter area. It is also necessary to use the instability interval for further determination. The criterion of the processing instability zone is given, which can be expressed as the following relationship:

$$\xi(\dot{\varepsilon})=\frac{\partial\ln[m/(m+1)]}{\partial\ln\dot{\varepsilon}}+m\le0 \tag{15}$$

where ξ the instability factor, and is a function of T and $\dot{\varepsilon}$. Similarly, the isoplethic curves of ξ can be drawn on the plane formed by the deformation temperature T and the strain rate $\dot{\varepsilon}$ (Fig. 6(b)). The negative $\xi(\dot{\varepsilon})$ value region represents flow instability.

The processing map can be constructed by the superposition of the instability on the power dissipation map, which can be used for processing parameter optimization and microstructure control in the hot working process. Figure 7(a) shows the hot processing map of N6 at a true strain of 0.5. The shaded part is the instability area, and the darker the color, the greater the degree of instability. The instability area refers to the region where the instability factor ξ is less than 0 in the instability diagram, which is the shaded part in the hot processing diagram. One main instability region exists in the processing map, where the temperature range of the instability region is 900−1050 °C, and the strain rate is 1−10 s^{-1}. The metallographic structure corresponding to the instability zone is shown in Fig. 7(b), which can be seen that larger elongated deformed grains (marked by the circle) are surrounded by fine dynamic recrystallized grains. The grain size in this region is not uniform, which may be the primary reason for the processing instability. The region where the value of η decreases sharply in the processing map is called the processing danger regions. The metallographic structures of processing danger regions I and II are shown in Figs. 7(d) and (e), respectively, which can be seen as severe grain coarsening, thereby reducing the processing performance of N6. The

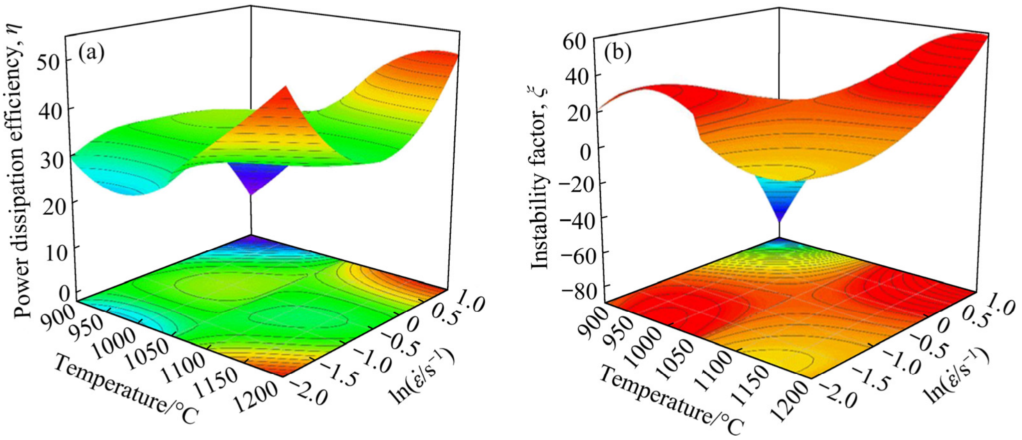

Fig. 6 Power dissipation map (a) and instability map (b) of N6 at true strain of 0.5

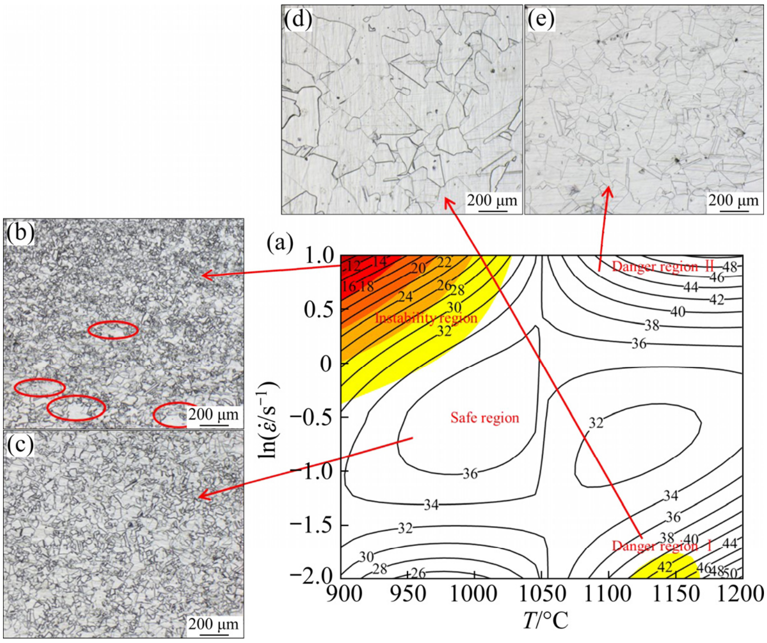

Fig. 7 Hot processing map (a) and corresponding metallographic structures (b−e) in different regions: (b) Instability region at 900 °C and 1 s^{-1}; (c) Safe region at 1000 °C and 1 s^{-1}; (d) Danger region I at 1200 °C and 0.01 s^{-1}; (e) Danger region II at 1200 °C and 10 s^{-1}

metallographic structure of the safe region is basically equiaxed, and the grain size is small and uniform (Fig. 7(c)). The range of the safe region is 900−1050 °C, and the strain rate is 0.1−1 s^{-1}. In summary, the establishment of hot processing map of N6 provides theoretical guidance to formulate reasonable hot processing parameters.

3.4 Microstructural and microtextural evolution

To study microstructural and microtextural evolution, EBSD observations were carried out on samples at strain rates of 0.01−10 s^{-1} and 900 °C, respectively. Figure 8 shows the orientation imaging microscopy (OIM) maps (a, c, e, g) and orientation angle distribution maps (b, d, f, h) at strain rates of 0.01−10 s^{-1} and 900 °C, respectively. The inset of orientation angle distribution maps is the grain boundary map, in which different colors represent different grain boundaries: the black line represents HAGBs, the red line is Σ3 twin grain boundaries (TBs), and the green line is sub-boundaries (SBs). As shown in Figs. 8(a) and (e), relatively high density SBs (<2°, indicated by green boundaries) are observed in large, deformed grains, which are surrounded by fine DRX grains. At the same time, some of the recrystallized grains have grown due to the lower strain rate. When the strain rates are 0.1 and 1 s^{-1} (Figs. 8(b) and (c)), it can be seen that the deformed grains are slightly elongated in the direction of the compression axis and some smaller equiaxed DRX grains are attached to the jagged grain boundaries of the deformed grains. The dynamic recrystallization structure is described as a "necklace structure", which confirms the occurrence of the DDRX mechanism during the hot working process [41,42]. When the strain rate is 10 s^{-1} (Fig. 8(d)), the elongated deformed grains have been replaced by DRX grains and the grain size is significantly larger than that under 0.1 and 1 s^{-1} conditions. From Fig. 8(e−h), it can be seen that the orientation angle distribution of hot-deformed N6 at different strain rates and 900 °C is basically bimodal, but the proportion of different types of GBs greatly varies. In addition, the distribution of Σ3 TBs is in the grain and near grain boundaries. Furthermore, the proportion of LAGBs decreases but that of HAGBs increases in the orientation angle distribution as the strain rate increases. From a microstructural point of view, the misorientation angle distribution is associated with the kinetics of dynamic recrystallization [43]. The increase in the average misorientation angle (θ_{Avg}) corresponds to the increase in volume fraction of DRX grains and vice versa. Specifically, θ_{Avg} increases from 26.956° (900 °C, 0.01 s^{-1}) to 40.921° (900 °C, 10 s^{-1}). The misorientation angle distribution and grain boundary maps of N6 at different strain rates and 900 °C clearly show that the evolution of the deformed grains is composed of entangled dislocations, subgrains, and LAGBs to the DRX grains.

Figure 9 shows that quantitative description of the microtextural evolution is presented by the sections (φ_2=0° and 45°) of orientation distribution functions (ODFs) at 900 °C and different strain rates. Since DRX occurs during hot deformation, the grains are characterized by relatively randomized orientation. Some ideal texture components are found during the hot deformation of N6, including shear $\{011\}\langle110\rangle$, Cu $\{112\}\langle111\rangle$, Goss $\{011\}\langle001\rangle$, and Brass $\{011\}\langle211\rangle$ [44].

The evolution characteristics of DRX volume fraction and the maximum intensity of all microtextural components at 900 °C and different strain rates are shown in Fig. 10. In the strain rate range of 0.01−10 s^{-1}, it can be found that the volume fraction of DRX grains increases with increasing strain rate. The acceleration of DRX at high strain rate was also observed in 800H alloy [45] and GH690 superalloy [46]. The maximum intensity of all microtextures displays a decreased tendency first and then an increased one with increasing DRX fraction, which implies that the level of DRX fraction plays an obvious role in strengthening the maximum intensities at the high strain rate of all the microtextural components in N6.

4 Discussion

Additional research must be performed to illustrate the specific DRX mechanism in hot deformation of N6. Furthermore, an in-depth understanding of the specific manifestation of different DRX mechanisms during the hot deformation of N6 is also imperatively needed.

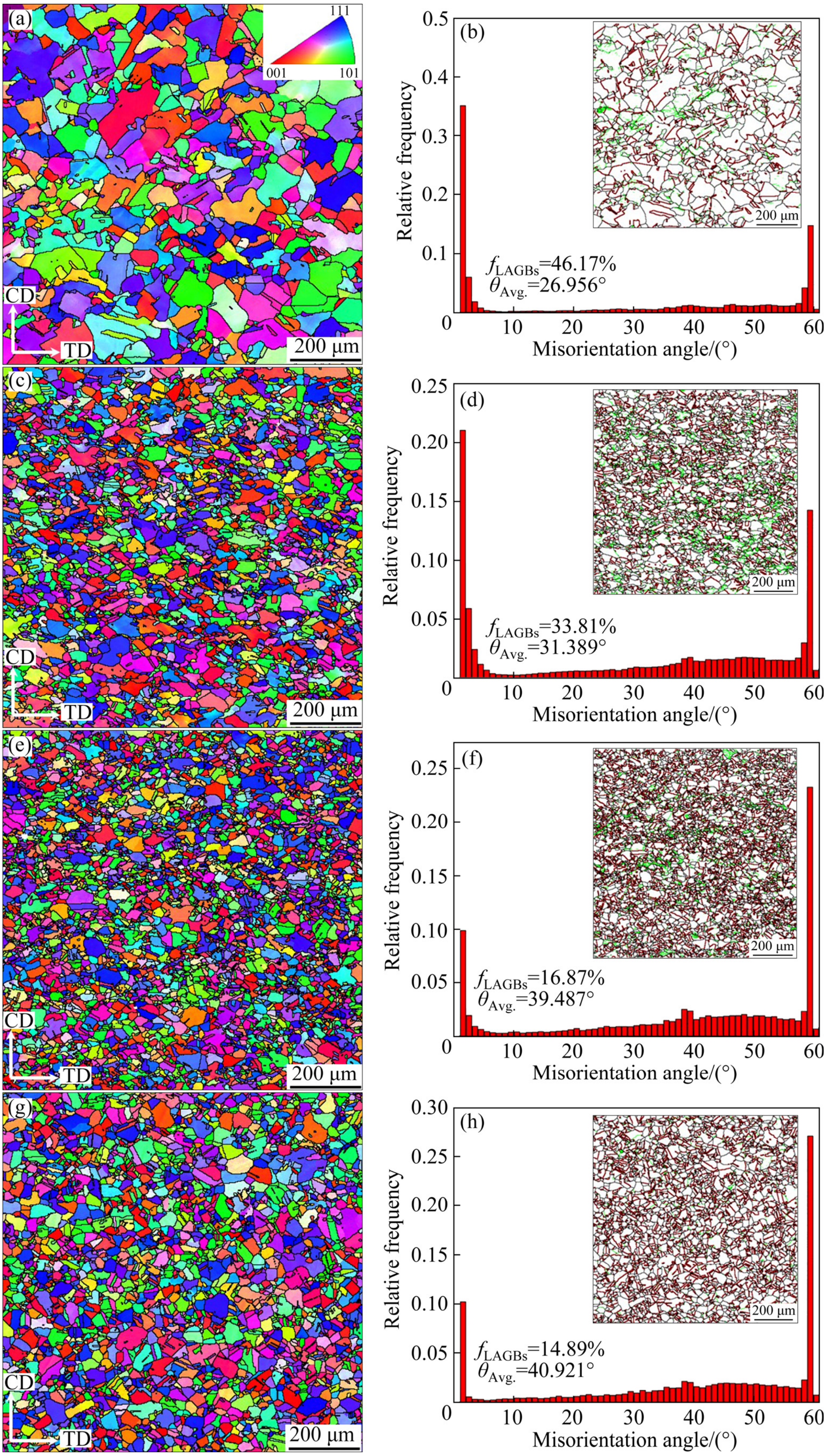

Fig. 8 OIM maps (a, c, e, g) and grain misorientation angle distributions (b, d, f, h) of N6 deformed at 900 °C and strain rates of 0.01 s^{-1} (a, b), 0.1 s^{-1} (c, d), 1 s^{-1} (e, f), and 10 s^{-1} (g, h)

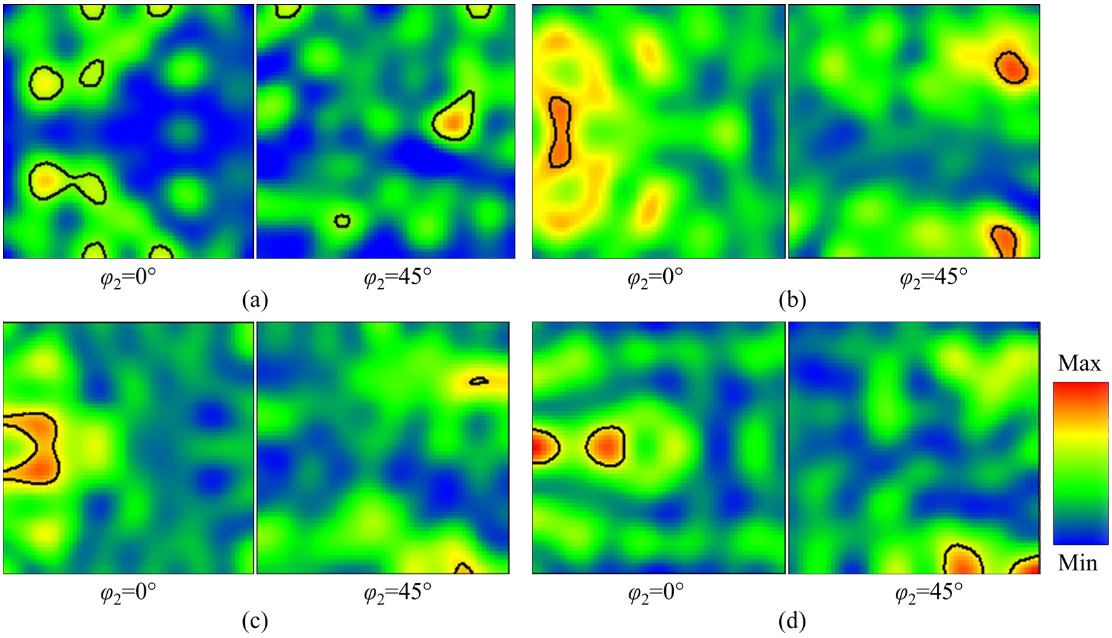

Fig. 9 ODF maps in Euler space of φ_2=0° and 45° under deformation conditions of different strain rates and 900 °C: (a) 0.01 s^{-1}; (b) 0.1 s^{-1}; (c) 1 s^{-1}; (d) 10 s^{-1}

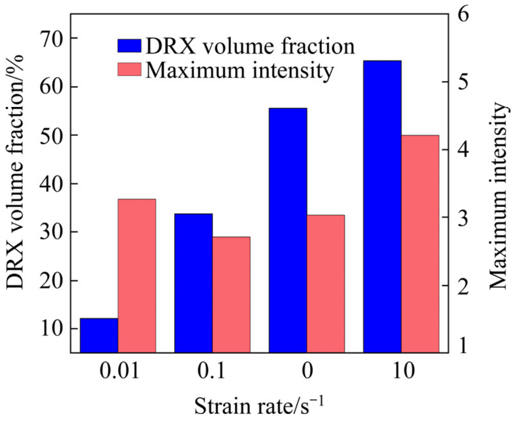

Fig. 10 Relationship between DRX volume fraction and maximum intensity of all microtextural components at 900 °C and different strain rates

4.1 Discontinuous dynamic recrystallization

4.1.1 Grain boundary bulging nucleation

DDRX is the main nucleation mechanism of nickel-based alloys, where bulging of the original HAGBs and the necklace structure consisting of DRX grains along the original HAGBs are its typical microscopic characteristics [16−18]. Figure 11 shows a partial IPF map of N6 under 900 °C and 0.1 s^{-1} hot deformation conditions. The typical necklace structure (marked by white ellipse) and strain-induced SBs (marked by white circle) can be observed in the microstructure of Fig. 11(a). Figure 11(b) shows an enlarged view of the white elliptical markers, and it can be observed from the microstructure in this figure that the initial HAGBs bulging position can be used as the actual nucleation position of DRX grains. To further characterize the orientation of DRX grains and parent grains, Grain 1 and Region 1 represent DRX grains and adjacent parent regions, respectively. The {111} pole figure in Fig. 11(c) shows the orientation relationship between Grain 1 and Region 1, where CD and TD represent the compression direction and transverse direction, respectively. Grain 1 and Region 1 are rotated 17.3° around the $[\bar{2}\bar{1}6]$ axis. When the HAGBs bulge due to different dislocation densities, the bulged region will inherit the orientation relationship of the parent grains [41]. Different rotational degrees of the bulging areas result in the transformation of the strain-induced sub-boundary between Grain 1 and Region 1 into the HAGBs. Thereby, DRX grains are formed.

4.1.2 Twin-assisted nucleation

Figures 12(a) and (b) reveal that most of the newly formed TBs are located inside the DRX grains, which indicates that twinning occurs during the growth stage of DRX grains. Twinning can reduce the boundary energy of growing grains and improve the mobility of grain boundaries [47,48], and the initial TBs will transform into HAGBs due

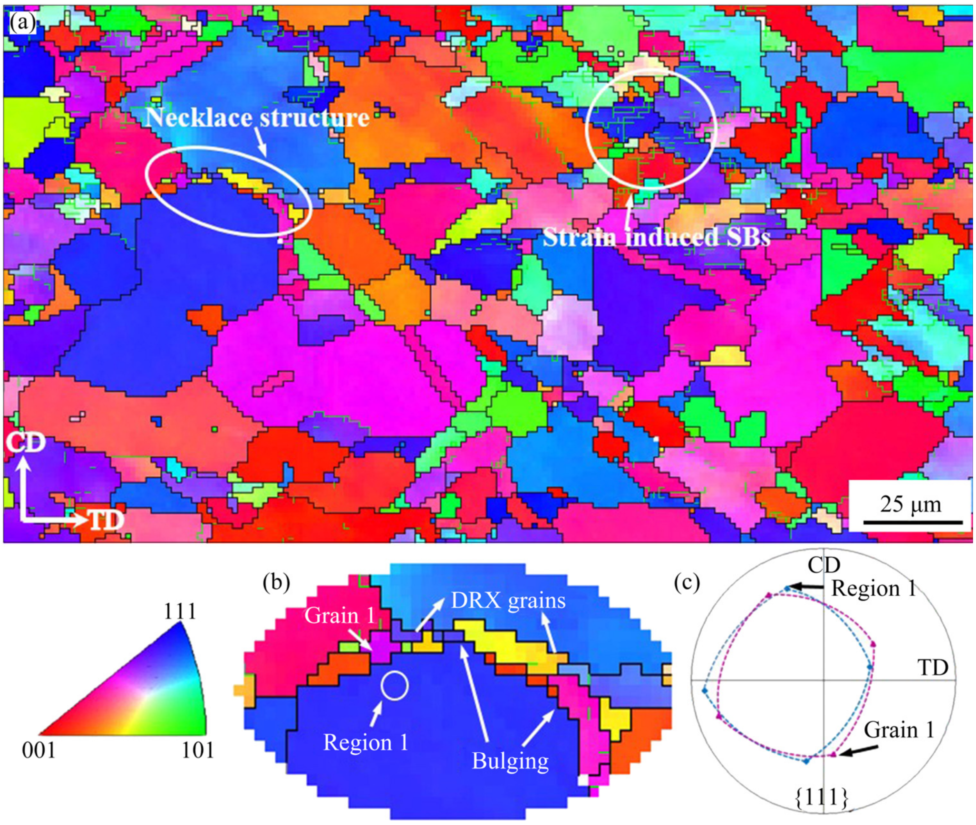

Fig. 11 Microstructure of N6 at 900 °C and 0.1 s^{-1} (a), enlarged view of necklace structure (b), and crystallographic relationship between Grain 1 and Region 1 (c)

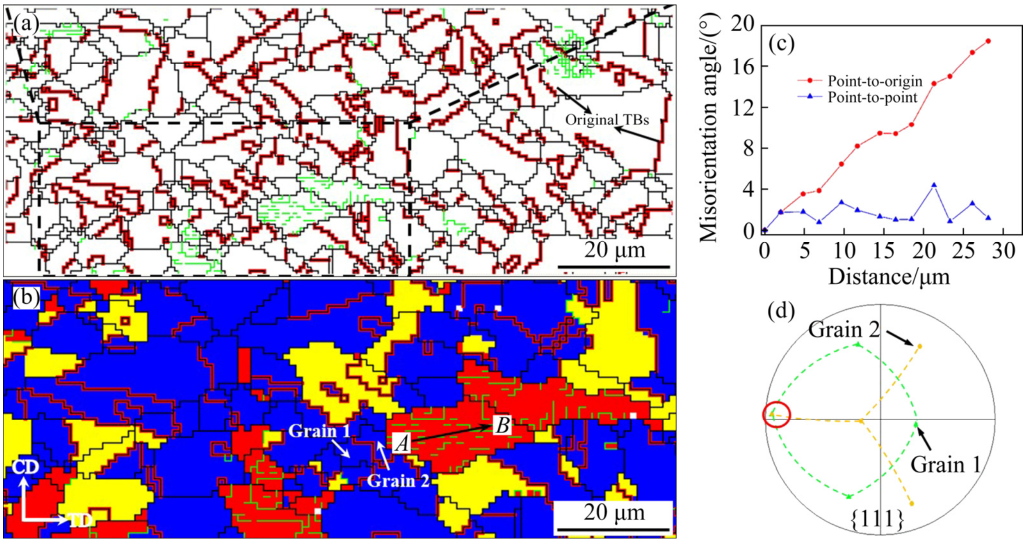

Fig. 12 Grain boundary map of N6 obtained at 900 °C and 0.1 s^{-1} (a), enlarged view of (a) marked by black rectangle (b), misorientation gradient measured along *AB* line (c), and crystallographic relationship between Grain 1 and Grain 2 (d)

to hot deformation. As shown in Fig. 12(b), the DRX grain with Σ3 boundary around the deformed grain is marked as Grain 1, and the grain adjacent to Σ3 boundary is marked as Grain 2. It can be seen from Fig. 12(d) that the orientation relationship of two grains is shown in the pole figure of {111}, and the overlapping point indicates the twin relationship between Grain 1 and Grain 2 on the {111} pole plane. Also, Grain 1 and Grain 2 are rotated 58.8° around the $[\bar{1}1\bar{1}]$ axis. Moreover, the misorientation angle of the coherent TBs is generally less than 1.7° away from ideal 60°/⟨111⟩, i.e., about one-fifth of the Brandon criterion for Σ3 (8.7°) [49]. At the same time, the deformed grains with SBs are attached to the GBs of Grain 2. As shown in Fig. 12(b), the Σ3 GBs in the DRX grains show the smallest distortion, while the deformed grains show a higher density of SBs. A line scan corresponding to the black arrow was conducted on the deformed grains and the measured misorientation profile is depicted in Fig. 12(c). The point-to-origin profile accumulates misorientations constantly, showing the high misorientation gradient. The difference in internal distortions of the two kinds of grains is the main driving force for grain boundary bulging, which allows the HAGBs to migrate. Therefore, twinning accelerates the DRX process.

4.2 Continuous dynamic recrystallization

Studies have shown that DDRX and CDRX often occur simultaneously in the process of hot deformation of nickel-based superalloys [16].

Figure 13(a) shows DRX distribution of N6 at 900 °C and 1 s^{-1}. Figure 13(b) shows a partial enlarged view of Region 1, and it can be seen that DRX grains with HAGBs are formed inside the initial deformed grains, which belongs to the typical nucleation mechanism that DRX grains are formed by progressive subgrain rotation. At the early stage of the formation of these DRX grains, some subgrains with an irregular shape in Region 2 are closed and semi-closed by LAGBs and HAGBs in Fig. 13(d). These subgrains in the circular area show a relatively wide span in the inverse pole map (Fig. 13(c)), which proves the occurrence of subgrains rotation inside the original deformed grains. In addition, Fig. 13(d) shows that the point-to-origin profile constantly accumulates misorientations based on measuring the point-to-point misorientation gradient of the *AB* line. During the subsequent deformation, through the increasing misorientation caused by progressive rotation of subgrains, these SBs first transit to MAGBs and then gradually change to HAGBs [50], so that DRX grains will be generated inside the initially deformed grains. Figure 13(e) is enlargement of Region 3. This is a typical DDRX mechanism, indicating that CDRX and DDRX occur simultaneously.

MAGBs are regarded to be a transition stage from LAGBs to HAGBs and the role of CDRX can be enhanced through the increased fraction of MAGBs [51,52]. Figure 14 shows the fractions of

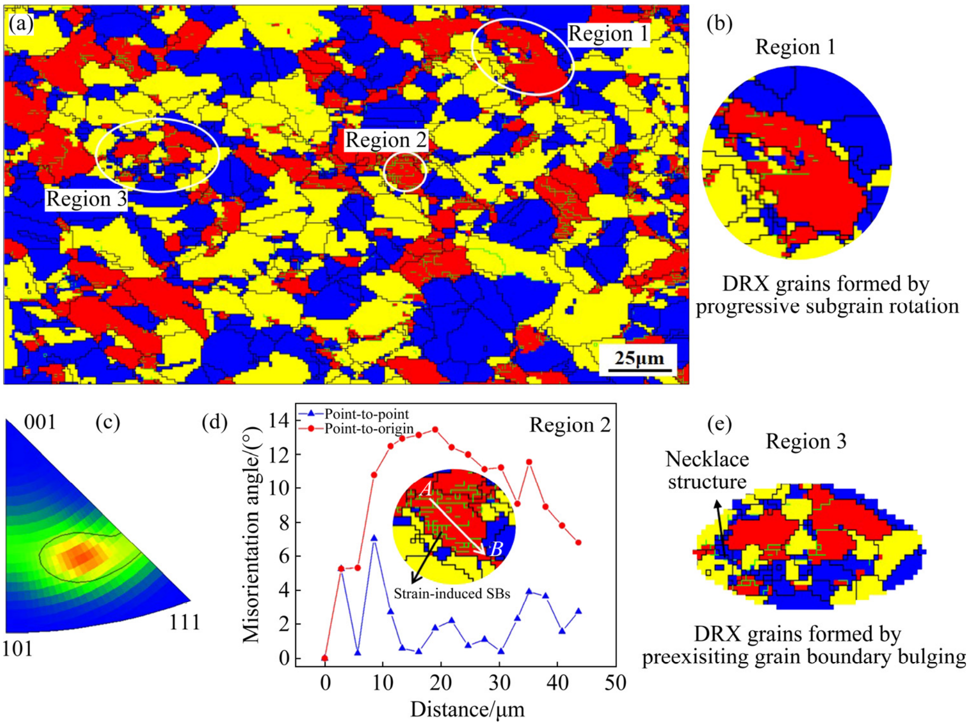

DRX grains formed by progressive subgrain rotation

DRX grains formed by preexisiting grain boundary bulging

Fig. 13 DRX distribution map of N6 at 900 °C and 1 s^{-1} (a), enlarged view of Region 1 (b), orientation relationships represented by inverse pole map of Region 2 (c), misorientation gradient of Region 2 measured along *AB* line (d), and enlarged view of Region 3 (e)

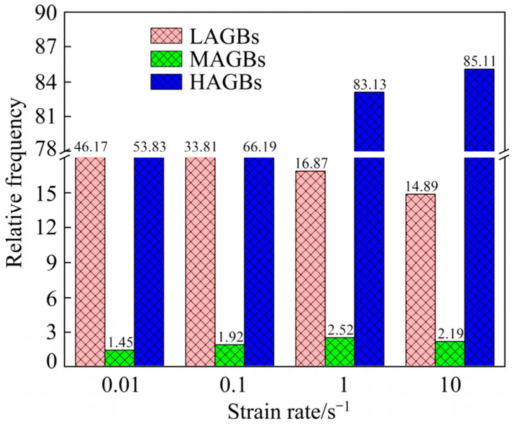

Fig. 14 Fractions of LAGBs, MAGBs and HAGBs at 900 °C and different strain rates

different types of GBs after hot compression at 900 °C and different strain rates. When the strain rate is less than 1 s^{-1}, the proportion of MAGBs increases with increasing strain rate, which indicates that the role of CDRX is enhanced with increasing strain rate. When the strain rate is greater than 1 s^{-1}, the fraction of MAGBs decreases with increasing strain rate, indicating that the role of CDRX is weakened. Studies have shown that the effect of CDRX is weakened by the increase in temperature [53]. Therefore, the reason for the weakening of the CDDX effect at 10 s^{-1} is the temperature rise effect in the hot deformation process with high strain rate. The fraction of MAGBs in Fig. 14 shows that the CDRX mechanism is more easily triggered at 900 °C and 1.0 s^{-1}. Although CDRX can be observed under the studied deformation conditions, the smaller fraction of MAGBs observed in this study clearly shows that the nucleation probability of CDRX is the lowest. Meanwhile, the fractions of HAGBs in Fig. 14 all show a considerable dominance under different conditions, which is also a characteristic of DDRX. Therefore, it is concluded that DDRX is a dominant DRX mechanism in N6, while CDRX is not an active one.

Figure 15 shows the typical TEM micrograph of N6 obtained at 900 °C and 1 s^{-1}. It can be seen from Fig. 15(a) that a large number of base plane slip bands (yellow lines) exist during the hot deformation process, which confirms that N6 is a

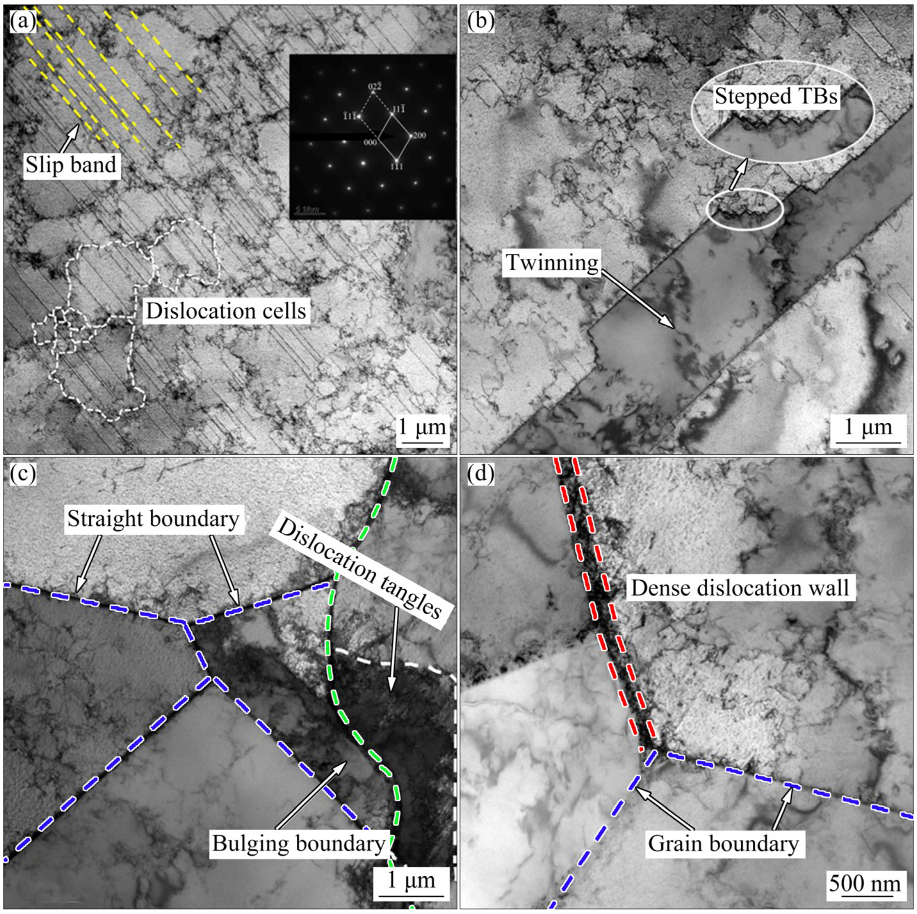

Fig. 15 TEM micrographs of dislocation cells (a), stepped twin (b), bulging boundary (c), and DDW (d) in specimen deformed at 900 °C and 1 s^{-1}

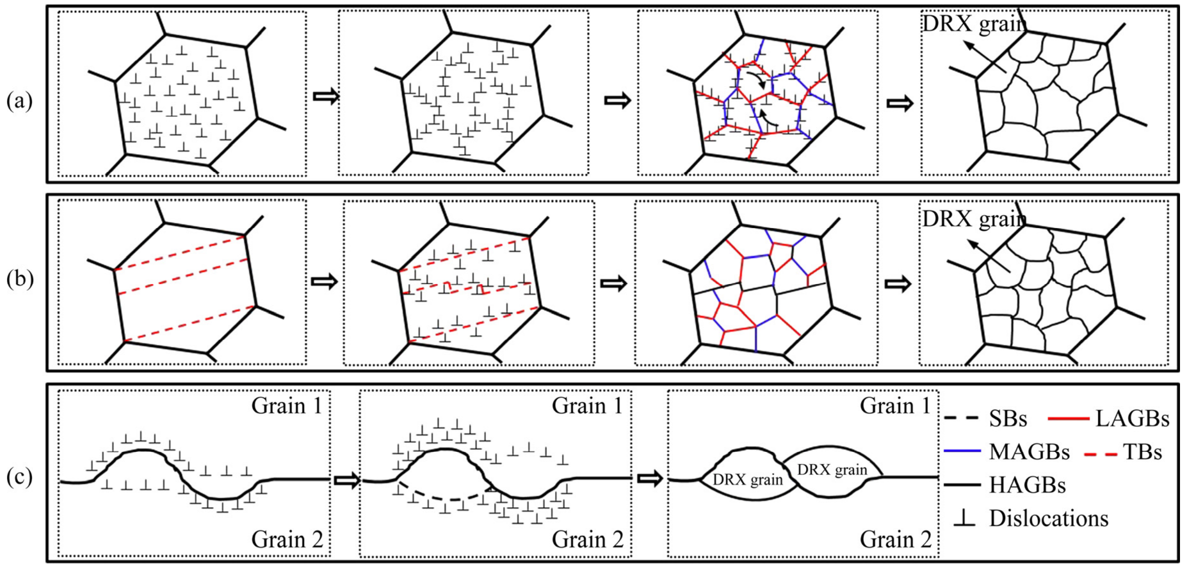

Fig. 16 Schematic diagrams of DRX mechanisms: (a) CDRX; (b, c) DDRX

plastic deformation mode dominated by slip, while a large number of dislocation tangles form dislocation cells with different sizes (marked by white dashed lines). The dislocation cells will transform into complete subgrains, and subgrains rotate and merge to form a DRX nucleus and then DRX grains are formed. Such a process is typical CDRX [6]. During hot deformation, the distorted twin boundaries can serve as preferential DRX nucleation sites [54]. It was found that TBs occurred via slip deformation, forming a stepped morphology (Fig. 15(b)). Strain fields surrounding the sharp edges of the twin steps give rise to local accumulation of dislocations and the formation of arrays of dislocation walls, which ultimately promote the nucleation of DRX [54]. The TEM image (Fig. 15(c)) confirms the existence of bulging boundaries (marked by the green dashed lines). The dislocation accumulation densities located at the bulging boundaries are much greater than that of the straight boundary (marked by the blue dashed line), which further confirms that bulging GBs will preferentially become the nucleation site. In addition, some dense dislocation walls (DDWs) (marked by red dashed line) of a few microns in length were observed (Fig. 15(d)), and the widths of the DDWs are rather narrow. The segmentation of original DDWs is the most common mechanism for the formation of new CBs [55]. Schematic diagrams for the above mentioned DRX mechanisms under the testing conditions for N6 are illustrated in Fig. 16.

5 Conclusions

(1) The flow behavior of N6 is significantly affected by the strain rate and deformation temperature. An obvious adiabatic temperature rise effect is generated at high strain rate (10 s^{-1}). The constitutive equation and processing map are built up from the temperature-corrected stress−strain curves.

(2) The optimal processing parameters for good workability are obtained in the temperature range of 950−1050 °C and strain rate range of 0.1−1 s^{-1}. Full DRX will occur under optimal conditions.

(3) The DRX process of N6 alloy is a thermally activated process and particularly sensitive to strain rate. At the same temperature, the degree of dynamic recrystallization is gradually strengthened with increasing strain rate. The adiabatic heat effect, high strain energy and dislocation density serve as vital reasons for the accelerated DRX at high strain rates.

(4) The DRX mechanism of N6 is shown as the dominant nucleation mechanism of DDRX characterized by grain boundary bulging and twin-assisted nucleation, while the CDRX characterized by subgrain combined with rotation is an inactive nucleation mechanism. In addition, the effect of CDRX nucleation strengthens first and then weakens with increasing strain rate.

Acknowledgments

This work was financially supported by the Science Foundation for Distinguished Young Scholars of Gansu Province, China (No. 18JR3RA134), Lanzhou University of Technology Support Plan for Excellent Young Scholars, China (No. CGZH001), and the National Nature Science Foundation of China (No. 51665032).

References

[1] GAO Ze-xi, JIA Zhi, JI Jin-jin, LIU De-xue, DING Yu-tian. Cold Deformation behavior and mechanical properties of forged pure nickel N6 [J]. Physics and Engineering of Metallic Materials, 2019, 217: 201−210.

[2] THELLAPUTTA G R, CHANDRA P S, RAO C S P. Machinability of nickel based superalloys: A review [J]. Materials Today: Proceedings, 2017, 4: 3712−3721.

[3] PALUMBO G, GONZALEZ F, BRENNENSTUHL A M, ERB U, SHMAYDA W, LICHTENBERGER P C. In-situ nuclear steam generator repair using electrodeposited nanocrystalline nickel [J]. Nanostructured Materials, 1997, 9: 737−746.

[4] GUYOT B M, RICHARDS N L. A study on the effect of cold rolling and annealing on special grain boundary fractions in commercial-purity nickel [J]. Materials Science and Engineering A, 2005, 395: 87−97.

[5] POLKOWSKI W, POLKOWSKA A, ZASADA D. Characterization of high strength nickel thin sheets fabricated by differential speed rolling method [J]. Materials Characterization, 2017, 130: 173−180.

[6] LIN Y C, WU Xian-yang, CHEN Xiao-min, CHEN Jian, WEN Dong-xu, ZHANG Jin-long, LI Lei-ting. EBSD study of a hot deformed nickel-based superalloy [J]. Journal of Alloys and Compounds, 2015, 640: 101−113.

[7] XIANG Xue-mei, JIANG He, DONG Jian-xin, YAO Zhi-hao. As-cast microstructure characteristic and homogenization of a newly developed hard-deformed Ni-based superalloy GH4975 [J]. Acta Metallurgica Sinica, 2020, 56(7): 988−996.

[8] YANG Pei-ru, LIU Chen-xi, GUO Qian-ying, LIU Yong-chang. Variation of activation energy determined by a modified Arrhenius approach: Roles of dynamic recrystallization on the hot deformation of Ni-based superalloy [J]. Journal of Materials Science & Technology, 2021, 72: 162−171.

[9] JIA Zhi, GAO Ze-xi, JI Jin-jin, LIU De-xue, GUO Ting-biao, DING Yu-tian. Study of the dynamic recrystallization process of the Inconel625 alloy at a high strain rate [J]. Materials, 2019, 12: 510−514.

[10] JIA Zhi, GAO Ze-xi, JI Jin-jin, LIU De-xue, GUO Ting-biao, DING Yu-tian. Texture evolution and dislocation behavior in a nickel-based superalloy during hot compression [J]. Advanced Engineering Materials, 2020, 22: 1900426.

[11] LIN Y C, WEN Dong-xu, DENG Jiao, LIU Guan, CHEN Jian. Constitutive models for high-temperature flow behaviors of a Ni-based superalloy [J]. Materials and Design, 2014, 59: 115−123.

[12] GUO Zhen-quan, PAN Jia, WANG Xuan. Prediction of the hot compressive deformation behavior for superalloy Nimonic 80A by BP-ANN model [J]. Applied Science, 2016, 6: 66−81.

[13] ZHANG Peng, HU Chao, ZHU Qiang, DING Chao-gang, QIN He-yong. Hot compression deformation and constitutive modeling of GH4698 alloy [J]. Materials and Design, 2015, 65: 1153−1160.

[14] XU Zhao-hua, LI Miao-quan, LI Hong. Plastic flow behavior of superalloy GH696 during hot deformation [J]. Transactions of Nonferrous Metals Society of China, 2016, 26: 712−721.

[15] JIA Zhi, GAO Ze-xi, JI Jin-jin, LIU De-xue, GUO Ting-biao, DING Yu-tian. High-temperature deformation behavior and processing map of the as-cast Inconel 625 alloy [J]. Rare Metals, 2021, 40: 2083−2091.

[16] WANG M J, SUN C Y, FU M W, LIU Z L, QIAN L Y. Study on the dynamic recrystallization mechanisms of Inconel 740 superalloy during hot deformation [J]. Journal of Alloys and Compounds, 2020, 820: 153325.

[17] AZARBARMAS M, AGHAIE-KHAFRIA M, CABRER J M, CALVOB J. Dynamic recrystallization mechanisms and twining evolution during hot deformation of Inconel 718 [J]. Materials Science and Engineering A, 2016, 678: 137−152.

[18] JIANG He, DONG Jian-xin, ZHANG Mai-cang, ZHENG Lei, YAO Zhi-hao. Hot deformation characteristics of alloy 617B nickel-based superalloy: A study using processing map [J]. Journal of Alloys and Compounds, 2015, 647: 338−350.

[19] WU Yu-ting, LI Chong, XIA Xing-chuan, LIANG Hong-yan, QI Qi-qi, LIU Yong-chang. Precipitate coarsening and its effects on the hot deformation behavior of the recently developed γ'-strengthened superalloys [J]. Journal of Materials Science & Technology, 2021, 67: 95−104.

[20] ZHANG Hong-bin, ZHOU Hai-ping, QIN Sheng-xue, LIU Jie, XU Xing-ming. Effect of deformation parameters on twinning evolution during hot deformation in a typical nickel-based superalloy [J]. Materials Science and Engineering A, 2017, 696: 290−298.

[21] WANG Y, SHAO W Z, ZHEN L, YANG L, ZHANG X M. Flow behavior and microstructures of superalloy 718 during high temperature deformation [J]. Materials Science and Engineering A, 2008, 497: 479−486.

[22] LIN Y C, HE Dao-guang, CHEN Ming-song, CHEN Xiao-min, ZHAO Chun-yang, MA Xiang, LONG Zhi-li. EBSD analysis of evolution of dynamic recrystallization grains and δ phase in a nickel-based superalloy during hot compressive deformation [J]. Materials & Design, 2016, 97: 13−24.

[23] WAN Zhi-peng, HU Lian-xia, SUN Yu, WANG Tao, LI Zhao. Microstructure evolution and dynamic softening mechanisms during high-temperature deformation of a precipitate hardening Ni-based superalloy [J]. Vacuum, 2018, 155: 585−593.

[24] ZHANG Hong-bin, ZHANG Kai-feng, JIANG Shao-song, ZHOU Hai-ping, ZHAO Chang-hong, YANG Xiao-li. Dynamic recrystallization behavior of a γ'-hardened nickel-based superalloy during hot deformation [J]. Journal of Alloys and Compounds, 2015, 623: 374−385.

[25] WANG Y, SHAO W Z, ZHEN L, ZHANG X M. Microstructure evolution during dynamic recrystallization of hot deformed superalloy 718 [J]. Materials Science and Engineering A, 2008, 486: 321−332.

[26] LIU Yan-hui, NING Yong-quan, YAO Ze-kun, LI Hui, MIAO Xiao-pu, LI Yu-zhi, ZHAO Zhang-long. Plastic deformation and dynamic recrystallization of a powder metallurgical nickel-based superalloy [J]. Journal of Alloys and Compounds, 2016, 675: 73−80.

[27] WU K, LIU G Q, HU B F, WANG C Y, ZHANG Y W, TAO Y, LIU J T. Effect of processing parameters on hot compressive deformation behavior of a new Ni−Cr−Co based P/M superalloy [J]. Materials Science and Engineering A, 2011, 528: 4620−4629.

[28] ROBERTS W, AHLBLOM B. A nucleation criterion for dynamic recrystallization during hot working [J]. Acta Metallurgica, 1978, 26: 801−813.

[29] SELLARS C M, MCTEGART W J. On the mechanism of hot deformation [J]. Acta Metallurgica, 1966, 14: 1136−1138.

[30] LIU Yi, HU Rui, LI Jin-shan, KOU Hong-chao, LI Hong-wei, CHANG Hui, FU Heng-zhi. Characterization of hot deformation behavior of Haynes230 by using processing maps [J]. Journal of Materials Processing Technology, 2009, 209: 4020−4026.

[31] JOHNSON G R, COOK W H. A constitutive model and data for metals subjected to large strains, high strain rates and high tem-peratures [C]//Proceedings of the 7th International Symposium on Ballistics. Hague, Netherlands, 1983: 541−548.

[32] SONG B, SANBORN B. A modified Johnson–Cook model for dynamic response of metals with an explicit strain- and strain-rate-dependent adiabatic thermosoftening effect [J]. Journal of Dynamic Behavior of Materials, 2019, 5: 212−220.

[33] GUO Peng-cheng, LI Luo-xing, LIU Xiao, YE Tuo, CAO Shu-fen, XU Cong-chang, LI Shi-kang. Compressive deformation behavior and microstructure evolution of AM80 magnesium alloy under quasi-static and dynamic loading [J]. International Journal of Impact Engineering, 2017, 109: 112−120.

[34] AHMAD I R, SHU D W. Compressive and constitutive analysis of AZ31B magnesium alloy over a wide range of strain rates [J]. Materials Science and Engineering A, 2014, 592: 40−49.

[35] WEN Dong-xu, LIN Y C, LI Hong-bin, CHEN Xiao-min, DENG Jiao, LI Lei-ting. Hot deformation behavior and processing map of a typical Ni-based superalloy [J]. Materials Science and Engineering A, 2014, 591: 183−192.

[36] QUAN Guo-zheng, LIU Qiao, ZHAO Jiang, WEI Xiong, SHI Rui-ju. Determination of dynamic recrystallization parameter domains of Ni80A superalloy by enhanced processing maps [J]. Transactions of Nonferrous Metals Society of China, 2019, 29: 1449−1464.

[37] WANG Ming-jia, WANG Wen-rui, LIU Zhong-li, SUN Chao-yang, QIAN Ling-yun. Hot workability integrating processing and activation energy maps of Inconel 740 superalloy [J]. Materials Today Communications, 2018, 14: 188−198.

[38] SRINIVASA N, PRASAD Y V R K. Hot working characteristics of nimonic 75, 80A and 90 superalloys: A comparison using processing maps [J]. Journal of Materials Processing Technology, 1995, 51: 171−192.

[39] PRASAD Y V R K, GEGEL H L, DORAIVELU S M, MALAS J C, MORGAN J T, LARK K A, BARKER D R. Modeling of dynamic material behavior in hot deformation: Forging of Ti-6242 [J]. Metallurgical Transactions A, 1984, 15: 1883−1892.

[40] PRASAD Y V R K. Processing maps: A status report [J]. Journal of Materials Engineering and Performance, 2003, 12: 638−645.

[41] SAKAI T K, BELYAKOV A, KAIBYSHEV R, MIURA H, JONAS J J. Dynamic and post dynamic recrystallization under hot cold and severe plastic deformation conditions [J]. Progress in Materials Science, 2014, 60: 130−207.

[42] LIN Y, CHEN X. A critical review of experimental results and constitutive descriptions for metals and alloys in hot working [J]. Materials & Design, 2011, 32: 1733−1759.

[43] GUO Qing-miao, LI De-fu, GUO Sheng-li, PENG Hai-jian, HU Jie. The effect of deformation temperature on the microstructure evolution of Inconel 625 superalloy [J]. Journal of Nuclear Materials, 2011, 414: 440−450.

[44] SUN Xuan, JIA Zhi, JI Jin-jin, WANG Yan-jiang, WEI Bao-lin, YU Li-dan. Microstructure evolution and texture characteristics of pure nickel N6 during cold rolling process [J]. Transactions of the Indian Institute of Metals, 2021, 74: 1361−1371.

[45] CAO Yu, DI Hong-shuang, ZHANG Jing-qi, ZHANG Jie-cen, MA Tian-jun, MISRAB R D K. An electron backscattered diffraction study on the dynamic recrystallization behavior of a nickel–chromium alloy (800H) during hot deformation [J]. Materials Science and Engineering A, 2013, 585: 71−85.

[46] SHI Zhao-xia, YAN Xiao-feng, DUAN Chun-hua, ZHAO Ming-han. Effect of strain rate on hot deformation characteristics of GH690 superalloy [J]. Transactions of Nonferrous Metals Society of China, 2017, 27: 538−550.

[47] GOTTSTEIN G. Annealing texture development by multiple twinning in f.c.c. crystals [J]. Acta Metallurgica, 1984, 32; 1117−1138.

[48] CORYELL S P, FINDLEY K O, MATAYA M C, BROWN E. Evolution of microstructure and texture during hot compression of a Ni−Fe−Cr superalloy [J]. Metallurgical and Materials Transactions A, 2012, 43: 633−649.

[49] MANDAL S, BHADURI A K, SUBRAMANYA SARMA V S. Role of twinning on dynamic recrystallization and microstructure during moderate to high strain rate hot deformation of a Ti-modified austenitic stainless steel [J]. Metallurgical and Materials Transactions A, 2012, 43: 2056−2068.

[50] YANUSHKEVICH Z, BELYAKOV A, KAIBYSHEV R. Microstructural evolution of a 304-type austenitic stainless steel during rolling at temperatures of 773−1273 K [J]. Acta Materialia, 2015, 82: 244−254.

[51] KUMAR S S S, RAGHU T, BHATTACHARJEE P P, RAO G A, BORAH U. Strain rate dependent microstructural evolution during hot deformation of a hot isostatically processed nickel base superalloy [J]. Journal of Alloys and

Compounds, 2016, 681: 28−42.

[52] LI De-fu, GUO Qing-miao, GUO Sheng-li, PENG Hai-jian, WU Zhi-gang. The microstructure evolution and nucleation mechanisms of dynamic recrystallization in hot-deformed Inconel 625 superalloy [J]. Materials & Design, 2011, 32: 696−705.

[53] GUO Qing-miao, LI De-fu, PENG Hai-jian, GUO Sheng-li, HU Jie, DU Peng. Nucleation mechanisms of dynamic recrystallization in Inconel 625 superalloy deformed with different strain rates [J]. Rare Metals, 2012, 31: 215−220.

[54] BELADI H, CIZEK P, HODGSON P D. Dynamic recrystallization of austenite in Ni−30PctFe model alloy: Microstructure and texture evolution [J]. Metallurgical and Materials Transactions A, 2009, 40: 1175−1189.

[55] LIU Q, JENSEN D J, HANSEN N. Effect of grain orientation on deformation structure in cold-rolled polycrystalline aluminium [J]. Acta Materialia, 1998, 46: 5819−5838.

纯镍 N6 的热加工性和动态再结晶机制

贾 智[1,2]，魏保林[1]，孙 璇[1]，姬金金[3]，汪彦江[1]，俞丽丹[1]

1. 兰州理工大学 材料科学与工程学院，兰州 730050；
2. 兰州理工大学 省部共建有色金属先进加工与再利用国家重点实验室，兰州 730050；
3. 兰州工业学院 材料工程学院，兰州 730050

摘　要：采用热压缩实验系统地研究纯镍 N6 的热加工性和动态再结晶机制。基于热压缩实验数据，建立 N6 的本构方程并验证其可靠性；构建其热加工图，结合显微组织观察建立热变形参数与显微组织之间的半定量响应关系。N6 的动态再结晶过程是一个热激活过程，对应变速率特别敏感。N6 的最佳热处理工艺参数确定为 950~1050 ℃和 0.1~1 s^{-1}。此外，还证明以晶界弓出和孪晶协助成核为特征的不连续动态再结晶机制是主要动态再结晶机制，而以亚晶旋转合并为特征的连续动态再结晶是辅助机制。

关键词：纯镍 N6；显微组织演变；热加工性；加工图；动态再结晶

(Edited by Wei-ping CHEN)